Degeneracy lifting due to thermal fluctuations around the frustration point between anticlinic antiferroelectric SmC_A^* and synclinic ferroelectric SmC^*

K. L. Sandhya,[1,*] A. D. L. Chandani,[1,2] Atsuo Fukuda,[1] Jagdish K. Vij,[1,3] A. V. Emelyanenko,[4] and Ken Ishikawa[5,†]

[1]*Department of Electrical and Electronic Engineering, Trinity College, University of Dublin, Dublin 2, Ireland*

[2]*Department of Chemistry, Faculty of Science, University of Peradenia, Peradenia, Sri Lanka*

[3]*School of Electronic and Electrical Engineering, Sungkyunkwan University, Suwon 440-476, Korea*

[4]*Department of Physics, Moscow State University, Moscow 119992, Russia*

[5]*Department of Organic and Polymeric Materials, Tokyo Institute of Technology, Tokyo 152-8552, Japan*

(Received 15 June 2012; revised manuscript received 19 October 2012; published 14 January 2013)

In the binary mixture phase diagram of MC881 and MC452, the borderline between anticlinic antiferroelectric SmC_A^* and synclinic ferroelectric SmC^* becomes apparently parallel to the temperature ordinate axis at the critical concentration r_c. The free energy difference between SmC_A^* and SmC^* is extremely small in a wide temperature range near r_c. In such circumstances, by observing Bragg reflection spectra due to the director helical structure and electric-field-induced birefringence, we have observed the continuous change from SmC_A^* to SmC^* for $r \lesssim r_c$ and the gradual growth of the full-pitch band over 5 °C or more in the apparent SmC^* temperature region for $r \gtrsim r_c$. These intriguing phenomena have been explained, successfully at least in the high-temperature region, by a thermal equilibrium between the synclinic and anticlinic orderings and the resulting Boltzmann distribution for the ratio between them; the thermal equilibrium is considered to be attained in a nonuniform defect-assisted way through solitary waves moving around dynamically. We have also discussed qualitatively an important role played by the effective long-range interlayer interactions in the low-temperature region.

DOI: 10.1103/PhysRevE.87.012502 PACS number(s): 61.30.Eb, 64.70.M−, 77.80.−e

I. INTRODUCTION

Just after the discovery of anticlinic antiferroelectric SmC_A^* [1], the phase transition between SmC_A^* and synclinic ferroelectric SmC^* was treated by simply considering such a free energy as

$$-\alpha(T - T_c)\cos\phi - Q\cos^2\phi. \quad (1)$$

Here, ϕ is the azimuthal angle difference of the in-layer directors between adjacent layers, T_c the phase transition temperature, and $\alpha > 0$ and $Q > 0$ are the temperature-independent constants [2]. This treatment has been frequently used ever since, in which the short-range interlayer interactions (SRILIs) alone are taken into account using the simple approximation of the perfect orientational and translational order [3,4]. Below T_c, SmC_A^* is stable with the minimum at $\phi = 180°$, whereas above T_c SmC^* becomes stable and the minimum at $\phi = 0$ is lower. Strictly speaking, the minimum occurs at $\phi = 180° + \delta_{AC}$ or $\phi = \delta_C$ because of the macroscopic helical structure of the director. Here, δ_{CA} and δ_C are both ca. 1° and have opposite signs [5–7]; the long pitch of the director helical structure typically encompasses hundreds of layers and may produce the Bragg reflections in the optical wavelength region. At $T = T_c$, a large number of superlattice structures characterized by the mixture of the synclinic ferroelectric and anticlinic antiferroelectric orderings must have the same free energy and hence are degenerate; both orderings are frustrated.

This degeneracy at the frustration point can be lifted either by weak long-range interlayer interactions (LRILIs) or by thermal fluctuations (entropy effects) [8–10]. Usually, we resort to the absolute zero temperature approximation and do not consider any thermal fluctuation effects. In fact, a series of electro-optical studies have revealed the degeneracy lifting which is considered due to LRILIs; chiral tilted smectic liquid crystals may exhibit a sequence of intermediate biaxial subphases around the frustration point between the main phases SmC_A^* and SmC^* with superlattice structures consisting of several smectic layers [11–16]. In particular, the three-layer ferrielectric and four-layer antiferroelectric Ising models were proposed by simply considering the flat structure. Here, we deal with the temperature region where the tilt angle is almost constant and large; hence, the optically uniaxial SmC^* variant, SmC_α^*, is outside the scope of our present consideration. Since the emergence of these biaxial subphases results from the frustration between SmC_A^* and SmC^*, and moreover since the ratio of the synclinic ferroelectric ordering in the unit cell

$$q_T = \frac{[F]}{[A] + [F]} \quad (2)$$

is $\frac{1}{3}$ in the ferrielectric three-layer subphase and $\frac{1}{2}$ in the antiferroelectric four-layer subphase, these are designated as Sm$C_A^*(\frac{1}{3})$ and Sm$C_A^*(\frac{1}{2})$, respectively. Notice that the emergence of intermediate biaxial subphases other than the ordinary ones, Sm$C_A^*(\frac{1}{3})$ and Sm$C_A^*(\frac{1}{2})$, are well established by the electro-optical studies, and that these subphases are also designated as Sm$C_A^*(q_T)$ [17–19]; with increasing temperature, q_T may increase monotonically from 0 for SmC_A^* to 1 for SmC^* since the degeneracy lifting is caused by weak LRILIs.

Resonant x-ray scattering (RXS) and some sophisticated electro-optical techniques have further revealed an intriguing and unexpected aspect of the biaxial subphase structure; the in-layer directors in a unit cell form a microscopic distorted helical structure with its short pitch [20–25]. Since the helix

*Present address: Dept of Physics, M. S. Ramaiah Institute of Technology, Bangalore-54, India.

†iken@op.titech.ac.jp

distortion is so large that the biaxial subphase structure is much closer to the Ising flat one [26–29], we can still unambiguously define the q_T number given in Eq. (2); we need to reinterpret $[F]$ and $[A]$ as the numbers of *quasi*synclinic ferroelectric and *quasi*anticlinic antiferroelectric orderings in a unit cell, respectively, though. The short pitch of the microscopic distorted helical structure, in the unit of the number of smectic layers, is given by

$$| p_{qT} | = \frac{2}{1 - q_T} \tag{3}$$

for a pair of the quasianticlinic antiferroelectric orderings makes one rotation. To be precise, the microscopic short-pitch distorted helical structure is not commensurate with the smectic layer since the biaxial subphases also have the macroscopic helical structure, the long pitch of which $p[\mathrm{Sm}C_A^*(q_T)]$ has been well established to be approximately given by

$$\frac{1}{p[\mathrm{Sm}C_A^*(q_T)]} = \frac{q_T}{p(\mathrm{Sm}C^*)} + \frac{1 - q_T}{p(\mathrm{Sm}C_A^*)}. \tag{4}$$

Here, the macroscopic helical long pitches of $\mathrm{Sm}C_A^*$ and $\mathrm{Sm}C^*$, $p(\mathrm{Sm}C_A^*)$ and $p(\mathrm{Sm}C^*)$, have the opposite signs [5–7].

The purpose of this paper is to report a very intriguing phenomenon: the degeneracy lifting due to disclination-assisted thermal fluctuations or linkages between the two orderings and the resulting apparently continuous change of q_T from 0 in $\mathrm{Sm}C_A^*$ to 1 in $\mathrm{Sm}C^*$. The phenomenon is observed in the binary mixture system studied by Song *et al.* [30], where the borderline between apparent $\mathrm{Sm}C_A^*$ and $\mathrm{Sm}C^*$ runs almost parallel to the ordinate temperature axis and hence we can define the critical concentration r_c. As pointed out above, we usually resort to the absolute zero temperature approximation and do not consider any thermal linkages between the two minima. Near the critical concentration r_c, however, the free energy difference between the minima must be extremely small over a very wide temperature range. This special situation seemed to be favorable in observing an unusual phenomenon. In fact, we observed the apparently continuous change of q_T from 0 in $\mathrm{Sm}C_A^*$ to 1 in $\mathrm{Sm}C^*$, and a preliminary paper has already been published [31].

In this paper, we study the mixture system more systematically by carefully changing the concentration near r_c and try to clarify the interplay between thermal fluctuations and LRILIs in the degeneracy lifting around the frustration point between $\mathrm{Sm}C_A^*$ and $\mathrm{Sm}C^*$. The mixture system shows a very favorable feature; the Bragg reflection due to the director helical structure is observed in the near-UV, visible, or near-IR wavelength region in the almost entire temperature range covering $\mathrm{Sm}C_A^*$ and $\mathrm{Sm}C^*$. Measuring the optical spectra of the Bragg reflection is one of the most useful nondestructive methods in studying the structure of easily deformable liquid crystalline systems. In this particular case of studying the frustration, much of the information comes from the presence or absence of the full-pitch band, i.e., the operating selection rules summarized in Fig. 1. What is really intriguing is the continuous growth of the full-pitch band observed in the apparently $\mathrm{Sm}C^*$ temperature region. The details will be explained in Secs. III A–III C, as spectral characteristics rather critically depend on the concentration, low, intermediate, and high. Several important issues will be raised in Sec. IV. In Sec. II, we will explain how carefully the spectral features were studied.

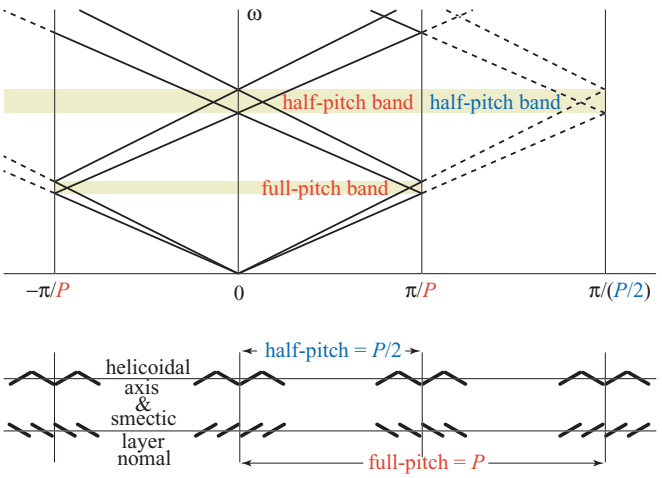

FIG. 1. (Color online) Dispersion relation for the Bragg reflection. The helicoidal periodicity is the full pitch in $\mathrm{Sm}C^*$, whereas it is the half pitch in $\mathrm{Sm}C_A^*$. Consequently, the Brillouin zones are $\pm\pi/P$ and $\pm\pi/(P/2)$, respectively; the second-order, ordinary characteristic reflections (half-pitch bands) are observed in both phases, but the first-order, total reflection (the full-pitch band) appears only in $\mathrm{Sm}C^*$. Notice that, even in $\mathrm{Sm}C^*$, light propagating along the helicoidal axis could not distinguish the tilting sense and hence it does not produce any full-pitch band; oblique incidence is necessary for observing the full-pitch band [1,32–34].

II. EXPERIMENT

The samples used are the binary mixtures of antiferroelectric MC881 and ferroelectric MC452, the chemical structures of which are given in Fig. 2. These were synthesized by Mitsubishi Gas Chemical Company, Inc., as the so-called "V-shaped switching materials" for grayscale displays [35–37]. In these references, some of the mixtures as well as MC452 were considered *ferrielectric* since the melatopes in conoscopy emerge parallel to the applied electric field. More recently, however, Song *et al.* unambiguously identified them to be ferroelectric [38]; the structural symmetry of $\mathrm{Sm}C^*$ allows either of melatopes parallel or perpendicular to the field, whereas the parallel melatopes inevitably appear in the ferrielectric $\mathrm{Sm}C_A^*(\frac{1}{3})$ subphase. We have tried to take adequate precautions in preparing mixtures of various concentrations because their properties critically depend on the mixing ratio near the critical concentration. Homeotropically

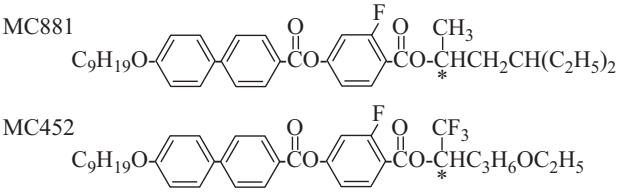

FIG. 2. The chemical formula for MC881 and MC452, both of which are (R) moieties.

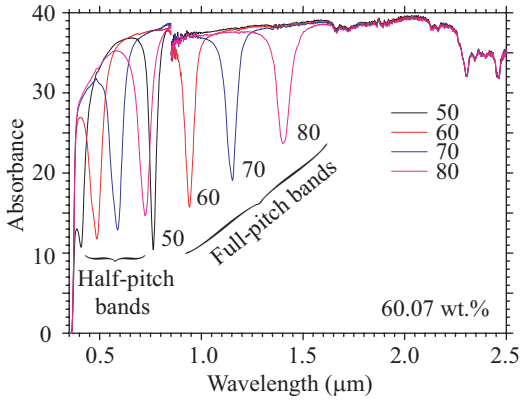

FIG. 3. (Color online) Bragg reflection spectra at indicated temperatures in the MC452 concentration of 60.07 wt%. Both half- and full-pitch bands are of single bell shape. The broad width and the multipeaked shape of Bragg reflection bands discussed in Secs. III and IV are to be compared with these narrow single-bell-shaped bands. The discontinuity at 0.85 μm is primarily caused by a detector change from photomultiplier to IR detector.

aligned, 25–50-μm-thick cells of these mixture samples were prepared using a Dow Corning 9-6346 Silane coupling agent, 72% octadecylaminodimethyltrimethoxy-silyl-propylammonium-chloride and 28% MeOH (methyl alcohol). The cell was mounted on a hot stage connected to a temperature controller, which regulates the temporal fluctuation within an accuracy of 0.01 °C or better but the spatial uniformity throughout the aperture of 1 mmϕ is ca. 0.1 °C. All the results presented, spectral and electric-field-induced birefringence (EFIB), were obtained by increasing temperature, unless otherwise stated.

The Bragg reflection bands of 50-μm homeotropic cells were obtained by measuring the transmittance spectra at an oblique incidence angle of 20° using a spectrophotometer (Lambda 900, PerkinElmer) covering near-UV, visible, and near-IR wavelength regions. We have prepared sample cells and measured the Bragg reflection spectra very carefully throughout these time-requiring and labor-intensive experiments. We insist that the broad width and the multipeaked shape of Bragg reflection bands near the critical concentration to be mentioned in Secs. III and IV are the intrinsic properties of the mixtures. Figure 3 serves to assure this point. It is the Bragg reflection spectra at several temperatures in the MC452 concentration of 60.07 wt% where the full-pitch band is always observed above 30 °C, the lowest temperature our oven arranges, and the special features for mixtures near the critical concentration r_c are not observed. Both half- and full-pitch bands are of single bell shape. The aforementioned broad width and the multipeaked shape are to be compared with these narrow single-bell-shaped bands. The slight discontinuity at 0.85 μm seen in Fig. 3 was caused by a detector change from photomultiplier to IR detector. The amount of discontinuity rather critically depended on how the sample was mounted, since the hot stage reduced the spectrophotometer aperture to 1 mmϕ for the sake of temperature uniformity.

The EFIB was measured in a homeotropically aligned cell by using a photoelastic modulator (PEM-90, Hinds Instruments, Hillsboro, OR). The cell consists of two glass plates separated by Mylar thin film spacers of 25-μm thickness, the bottom plate of which has two ITO (indium tin oxide) stripes as electrodes separated 180 μm apart. A He-Ne laser with wavelength of 632.8 nm and continuous-wave (cw) output power of about 2 mW was used as the light source for the EFIB measurements. Details were explained in previous papers [17,18,39].

III. RESULTS

The global temperature-concentration (T-r) phase diagram for the binary mixture system of MC881 and MC452 was determined in homeotropically aligned cells thicker than 25 μm by measuring the real part of the dielectric permittivity, the Bragg reflection, and/or the EFIB [30,31]. The phase boundary does not appear to depend on the cell thickness so long as the thickness is larger than 25 μm. There was no difficulty in pinpointing the boundaries between SmA and isotropic and between SmC^* and SmA with practically negligible thermal hysteresis. It is not straightforward, however, to determine the boundary between SmC_A^* and SmC^*, for thermal hysteresis becomes crucial. Moreover, the dielectric response gradually changes between them even in thick cells as seen in Fig. 6 of Ref. [30]. Consequently, Song *et al.* measured EFIB to draw the E–T phase diagram and found the three-layer subphase Sm$C_A^*(\frac{1}{3})$. They considered that it emerges stably in a finite temperature range even at zero electric field and causes the gradual change of the dielectric response between SmC_A^* and SmC^*; however, the stable existence of Sm$C_A^*(\frac{1}{3})$ apparently contradicts the continuous moving of the Bragg reflection peak toward the longer wavelength side across the temperature region supposed to be in Sm$C_A^*(\frac{1}{3})$, as pointed out in the previous paper [31]; we will also try to understand this apparent discrepancy more in detail in this paper.

Figure 4 summarizes the so-far studied temperature dependence of the Bragg reflection peak for various MC452 concentrations near r_c. The reflection spectra were observed in the heating process from 30 °C. Measurements below room temperature could not be made in our temperature-controlled oven used for electro-optical experiments. The studies are rather systematic, but not complete, for it takes a very long time to perform such measurements. The patterns of the peak wavelength versus temperature can be broadly divided into three types according to the MC452 concentration regions: (A) low, (B) intermediate, and (C) high as shown in Fig. 4. Figure 5(a) is the temperature-concentration (T-r) phase diagram. Song *et al.* studied this mixture system [30], but results close to r_c are newly obtained and they are presented in Fig. 5(b). Although it is basically impossible to specify the phase transition temperature between SmC_A^* and SmC^* in the mixture system here investigated as pointed out in the previous preliminary paper [31], we plotted the temperature range as an upward arrow where the full-pitch band emerges and shows a remarkable growth as temperature rises. Another indicator must be the temperature where the peak wavelength of the half-pitch band diverges, which is also plotted there, if it exists. Figure 5 is helpful to see the distribution of studied concentrations and the aforementioned three regions (A), (B), and (C).

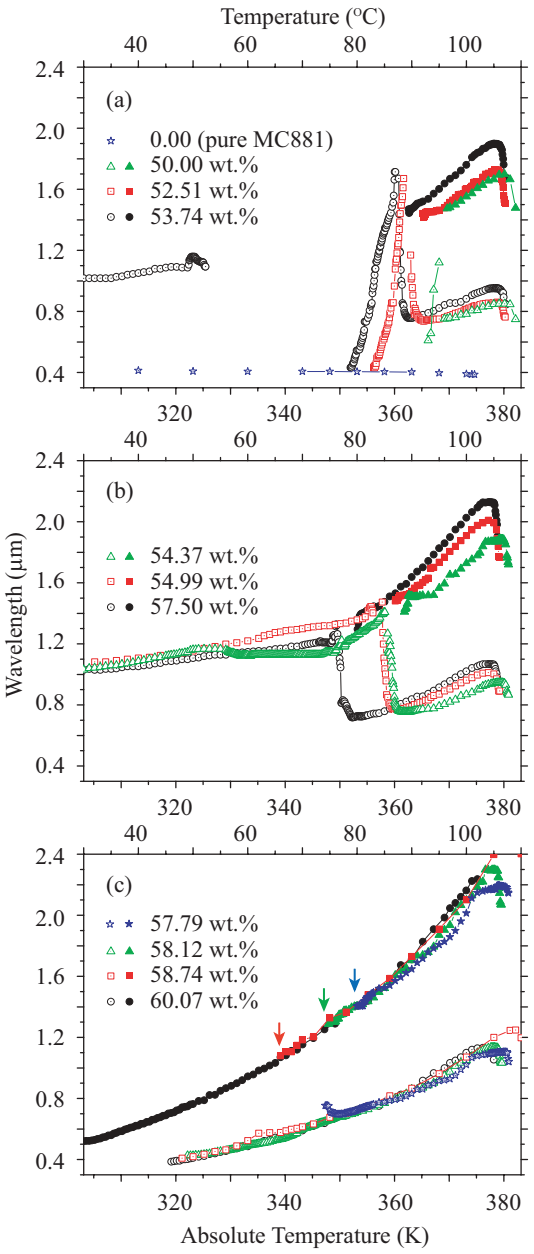

FIG. 4. (Color online) Temperature dependence of the Bragg reflection peak at various MC452 concentrations near r_c. Open symbols are for half-pitch bands and closed ones for full-pitch bands. The patterns of the peak wavelength vs temperature can be broadly divided into three types (a), (b), and (c) according to the MC452 concentration regions: (A) low, (B) intermediate, and (C) high. Arrows indicate the temperatures where the full-pitch bands start to grow.

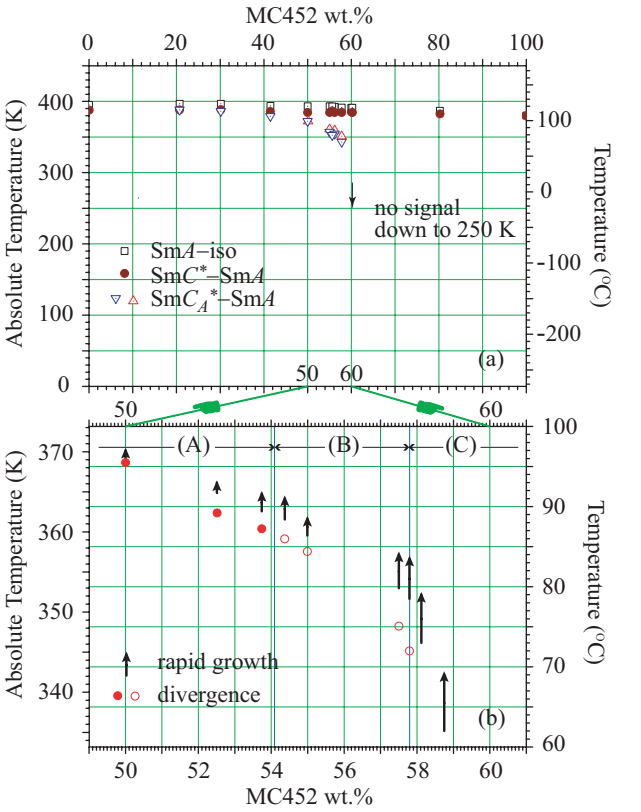

FIG. 5. (Color online) (a) Bulk phase diagram of MC881-MC452 binary mixture system and (b) expanded one near the critical concentration r_c indicating an apparent boundary between SmC_A^*-like and SmC^*-like states. We plotted the temperature ranges as upward arrows where the full-pitch band emerges and shows a rapid growth as the temperature rises, for it is basically impossible to specify the phase transition temperature between SmC_A^* and SmC^*. When the divergence or its indication can be seen in the half-pitch band, the temperatures are also given as red circles: closed ones in the case of a steep half-pitch rise on both the low- and high-temperature sides, while open ones in the case of a clear rise on the high-temperature side only. Concentration regions (A), (B), and (C) correspond to those in Fig. 4, respectively.

A. Low-concentration type

No SmC^* exists and the direct transition between SmC_A^* and SmA occurs in pure MC881; the half-pitch band of SmC_A^* is observed at about 0.4 μm with right-handed circular polarization for normal incidence. As the concentration of MC452 increases, the half-pitch band moves toward the shorter-wavelength side and comes to be buried under the intrinsic absorption even in the 10 wt% mixture. In the MC452 concentrations of 50.00, 52.51, and 53.74 wt% in Fig. 4(a), therefore, it is natural to consider that most of the low-temperature region apparently represents SmC_A^* since no reflection band is observed, aside from the near-IR reflection band at around 1.05–1.1 μm observed between 30 °C–49 °C in 53.74 wt%, the details of which will be given later. In the high-temperature region, on the other hand, the full-pitch band as well as the half-pitch band are observed, and hence SmC^* may apparently appear. In-between high and low, there is an intermediate-temperature region where the half-pitch band shows a remarkable change. With rising temperature, the half-pitch band comes to be observed starting from the tail of the intrinsic absorption band and moves toward the longer-wavelength side. The peak wavelength diverges at a particular temperature, which depends on the MC452 concentration; the bandwidth abruptly increases at the same time. After the divergence occurs, a very broad band comes to be observed again, and the peak wavelength as well as the bandwidth abruptly decreases. The half-pitch band is right

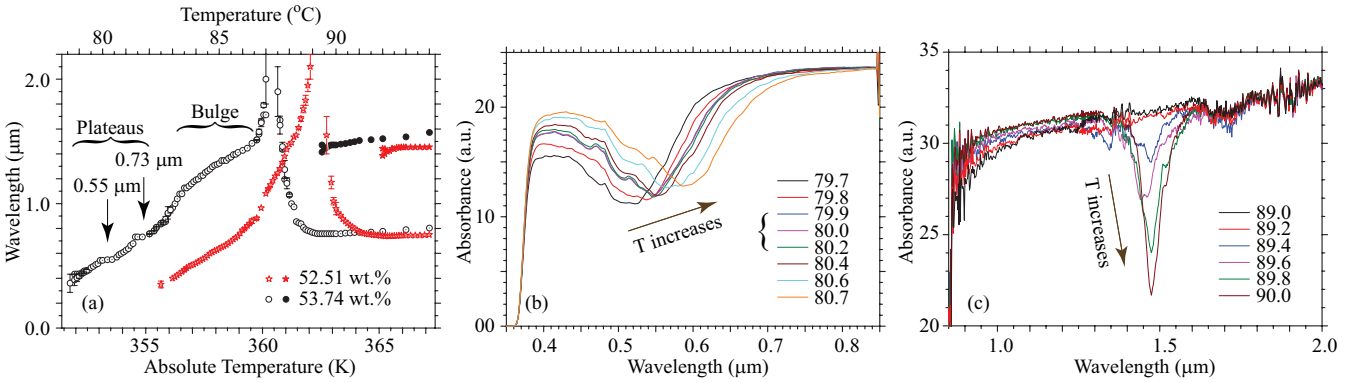

FIG. 6. (Color online) Temperature dependence of the Bragg reflection bands: (a) peak wavelength vs temperature, where two plateaux and a bulge are seen conspicuously in 53.74 wt% but not in 52.51 wt%; open and closed circles represent the half- and full-pitch bands, respectively; (b) illustration of three spectra at 79.9 °C, 80.0 °C, and 80.2 °C that look like almost the same in 53.74 wt%; and (c) illustration of characteristic rapid growth of the full-pitch band over ∼1 °C in 53.74 wt%.

circularly polarized on the low-temperature side of the divergence while left circularly polarized on the high-temperature side.

Figure 6 is the summary of a rather detailed spectroscopic study performed for 53.74 wt% in this paper. While the half-pitch band moves toward the longer-wavelength side with rising temperature, two plateaux appear at 0.55 μm (79.9 °C–80.2 °C) and 0.73 μm (81.4 °C–81.7 °C) as indicated in Fig. 6(a), where the band shape as well as the peak does not change very much within a finite temperature range as illustrated in Fig. 6(b). A bulge on the curve is also observed around 1.0–1.5 μm (83 °C–86.5 °C) as already pointed out in the preliminary paper [31]. As the temperature rises beyond the half-pitch divergence, the full-pitch band begins to grow in a characteristic manner as illustrated in Fig. 6(c). It emerges first as a very broad, multipeaked band and then grows rapidly into an almost bell-shaped, ordinary full-pitch band; this occurs within a temperature range as narrow as ∼1 °C. The Bragg reflection spectra in 52.51 wt% were also studied rather in detail here and confirmed the similar global behavior: the peak divergence of the half-pitch band and the characteristic growth of the full-pitch band. At the same time, some differences were noticed: (i) the overall intermediate temperature range becomes narrower; (ii) the near-IR reflection band at around 1.05–1.1 μm (30 °C–49 °C) does not emerge; and (iii) any plateaux and bulge are not conspicuously observed on the low-temperature side of the divergence.

In the previous paper for 53.74 wt% [31], we reported (i) the contours in the E–T phase diagram show a valley (the most easily deformable region), which indicates the stabilization of Sm$C_A^*(\frac{1}{3})$ in an applied electric field, on the low-temperature side of the divergence; (ii) the contours suggest that the temperature region of the apparent SmC^* prevails on the high-temperature side of the valley, where the half-pitch divergence and the full-pitch-band growth is observed; (iii) the contours just below the valley, on the other hand, seem to indicate the possible effects of several metastable subphases, for EFIB as large as 1×10^{-3} or less can hardly be produced in SmC_A^* in the field strength range indicated. Not only in 53.74 wt% but also in 52.51 wt%, we obtained the similar E–T phase diagram in the present studies.

Since the plateaux are observed as shown in Fig. 6(a), we tried to confirm that the valley really corresponds to the bulge but not to one of the plateaux at 0.73 μm (81.4 °C–81.7 °C) in 53.74 wt%. So far, however, we are not successful and the relation between the valley in the E–T phase diagram and the plateaux in Fig. 6(a) remains to be confirmed in the future. The difficulty lies in the fact that the emerging temperatures of the valley and the plateau critically depend on the sample thermal history. It must be necessary to measure the spectra and EFIB at the same time by changing the temperature at a step of 0.1 °C. Because of the stability of our EFIB-measuring system and the very wide temperature range to be studied, we had to change the temperature at a step of 0.5 °C so that the valley might appear at a temperature 84.0 °C, slightly higher than the 0.73-μm (81.4 °C–81.7 °C) plateau. In this low-temperature resolution, the bottom of the valley is indeed not flat but is pointed sharply downwards as shown in Fig. 7. Notice that

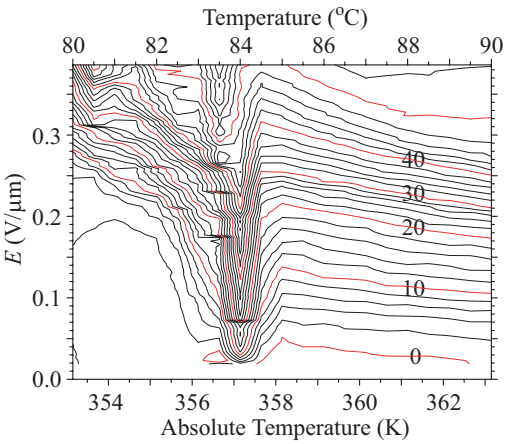

FIG. 7. (Color online) E–T phase diagram with EFIB contours in a 25-μm homeotropic cell in 53.74 wt%. The contour lines are drawn at a step of $\Delta n = 2 \times 10^{-3}$, and marked are the values of birefringence Δn multiplied by 10^{-3}. EFIB was measured at a particular temperature by changing the applied field stepwise at an interval of 8.33 mV μm^{-1} and the temperature was raised at a step of 0.5 °C.

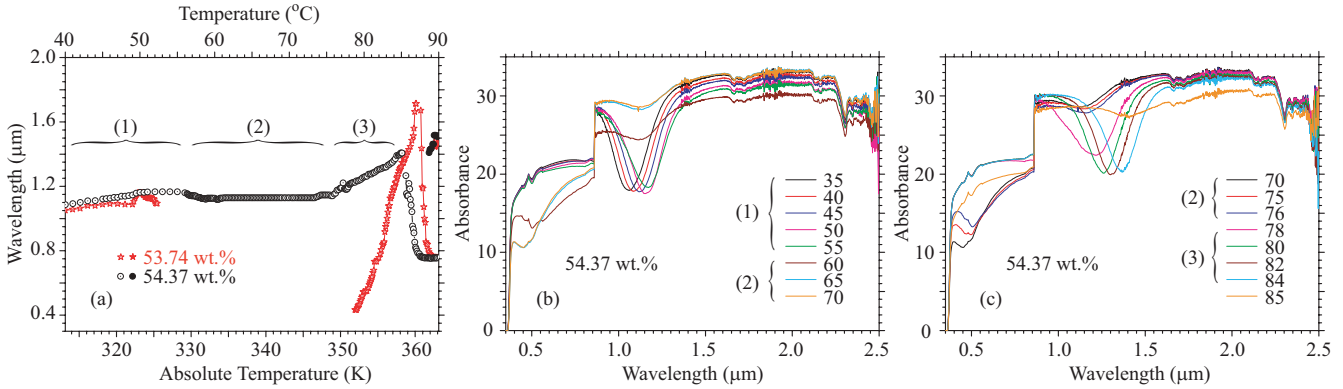

FIG. 8. (Color online) Bragg reflection bands at various temperatures indicating a continuous change from 53.74 to 54.37 wt%: (a) peak wavelength vs temperature in 53.74 and 54.37 wt%, where the indicated temperature ranges are (1) 30 °C–55 °C, (2) 56 °C–77 °C, and (3) 78 °C–84.5 °C, respectively; (b) reflection bands observed at around 1.05–1.1 μm (30 °C–55 °C) in 54.37 wt%; and (c) reflection bands observed at around 1.2–1.35 μm (78 °C–84.5 °C) in 54.37 wt%. The discontinuity at 0.85 μm is caused by a detector change from photomultiplier to IR detector.

the plateaux were successfully observed when the spectra were measured from 0.35 to 2.5 μm with a slow scanning speed by increasing the temperature from 30 °C to 100 °C at a step of 0.1 °C.

B. Intermediate-concentration type

The peak wavelength versus temperature curve in 54.37 wt%, at first glance, looks completely different from that in 53.74 wt%. When we observe the differences carefully, however, the change can be considered continuous. A clue is given by the 54.37 wt% Bragg reflection bands at various temperatures illustrated in Fig. 8. Broadly speaking, the region below the temperature where the peak wavelength diverges is divided into three parts: (1) 30 °C–55 °C, (2) 56 °C–77 °C, and (3) 78 °C–84.5 °C. As seen in Figs. 8(a) and 8(b), the 54.37 wt% bands in the temperature region of (1) 30 °C–55 °C look like the same as the 53.74 wt% ones in the temperature region of 30 °C–49 °C. Likewise, the 54.37 wt% bands in the region of (3) 78 °C–84.5 °C is quite similar to the 53.74 wt% ones shown in Fig. 4(a) of Ref. [31] in the region of 83 °C–86.5 °C, where the bulge is observed in the peak wavelength versus temperature curve shown in Fig. 6. In the in-between region of (2) 56 °C–77 °C, the bands are not single-bell-shaped ones, implying that the director helical structure must be complicated. By slightly increasing the MC452 concentration, this in-between (2) region disappears and (1) region continuously changes into (3) region as seen in 54.99 and 57.50 wt% shown in Fig. 4. Consequently, the director structure in (1) and (3) regions must bear some resemblance. It should be noticed that, in the intermediate-concentration region, the divergence behavior of the peak wavelength does not occur typically as in the low-concentration region.

C. High-concentration type

On increasing the MC452 concentration from 57.50 to 57.79 wt%, although the concentration difference is only 0.29 wt%, the change in Bragg reflection spectra at lower temperatures is drastic; the near-IR Bragg reflection band at around 1.05–1.35 μm (30 °C–84.5 °C) is clearly observed in the intermediate concentration region as well as in 57.50 wt% as shown in Figs. 4, 8, and 9, whereas no reflection band emerges in 57.79 wt% as is clearly seen by comparing

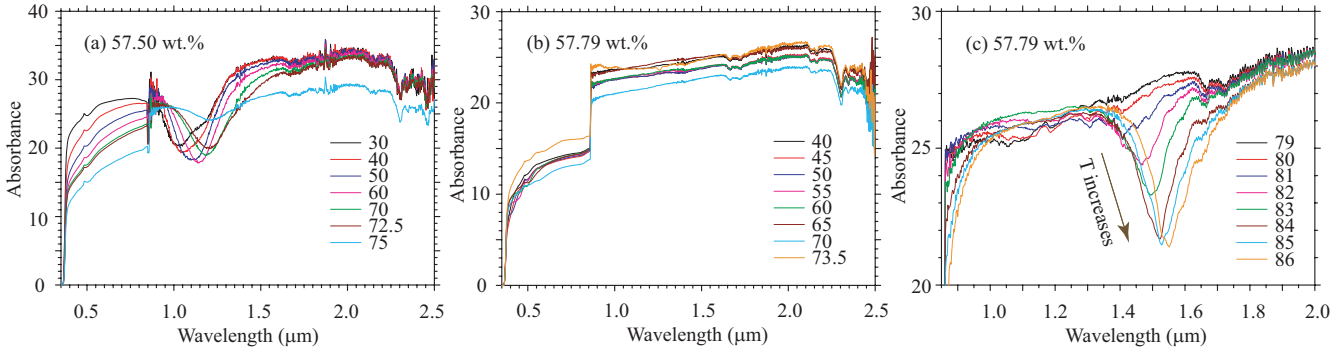

FIG. 9. (Color online) Bragg reflection spectra indicating a drastic change produced by slightly increasing the MC452 concentration: (a) reflection bands at around 1.05–1.2 μm (30 °C–75°C) in 57.50 wt%; (b) reflection spectra showing no bands at around 40 °C–70°C in 57.79 wt%; (c) characteristic growth of the full-pitch band over a temperature range as wide as ∼5 °C in 57.79 wt%. The discontinuity at 0.85 μm is caused by a detector change from photomultiplier to IR detector.

Figs. 9(a) and 9(b). At higher temperatures, no drastic change occurs and not only the half-pitch band but also the full-pitch band are ordinarily observed as plotted in Figs. 4(b) and 4(c). It deserves special notice, however, that both half- and full-pitch bands in 57.79 wt% are much broader than those in slightly lower 57.50 and slightly higher 58.12 wt%, and that the full-pitch band grows over a very wide temperature range of 5 °C or more as shown in Fig. 9(c). The temperature range is less than 1 °C in 53.74 wt% as shown in Fig. 6(c) and becomes wider as the MC452 concentration increases. At around 73 °C in Fig. 4(c), we can see a trace of the divergence behavior, which is conspicuously observed on both high- and low-temperature sides in 52.51 and 53.74 wt% and less conspicuously only on the high-temperature side in the intermediate concentration region as seen in Figs. 4(a) and 4(b).

On further increasing the MC452 concentration, even the trace of the divergence could not be observed in 58.12 wt% or higher, but the full-pitch band does not emerge at low temperatures. In 60.07 wt%, however, the full-pitch band comes to always emerge clearly at temperatures above 30 °C, the lowest temperature where the electro-optical measurements were performed actually; moreover, the dielectric measurements down to −20 °C that were made with a different hot stage did not detect any abrupt change for a phase transition, either. Although it is not clear whether the boundary becomes exactly parallel to the temperature ordinate axis, yet it is natural to consider that there exists a concentration range above ca. 60 wt% where SmC^* is stabilized absolutely even at lower temperatures instead of SmC^*_A. It should be noted that the E–T phase diagram for 54.37 wt% in the intermediate temperature region does show a valley (the most easily deformable region), a feature of stabilization of Sm$C^*_A(\frac{1}{3})$ in an applied electric field, on the low-temperature side of the divergence as seen in Fig. 10(a), whereas the diagram illustrated in Fig. 10(b) does not show the valley for 57.79 wt%.

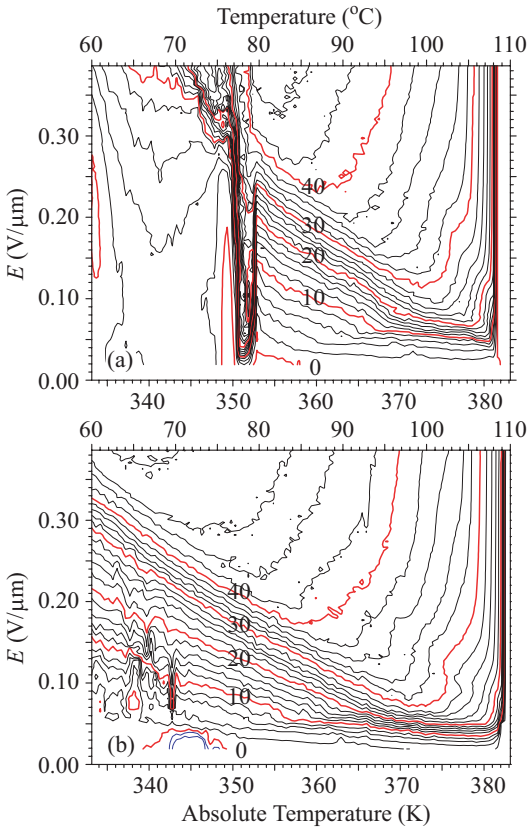

FIG. 10. (Color online) E–T phase diagrams with EFIB contours in a 25-μm homeotropic cell in (a) 54.37 wt% and (b) 57.79 wt%; a valley (the most easily deformable region) emerges at around 78 °C in (a), but no valley is observed down to 60 °C in (b).

IV. DISCUSSION

A. Degeneracy lifting due to LRILIs

Any long-range interlayer interactions (LRILIs) do lift the degeneracy at the frustration point and consequently stabilize some of the superlattice structures to exist as intermediate biaxial subphases in finite temperature ranges between the main phases SmC^*_A and SmC^* [8–10]. Several theoretical models for the LRILIs have been proposed, which can predict the emergence of subphases other than the typical ones with three- and four-layer superlattice structures [35,40–46]. Here, we try to understand the observed features in terms of the effective LRILIs introduced in Ref. [43]. It is the only model that can reasonably explain the staircase character of the subphase emergence as well as the microscopic short-pitch distorted helical structures of the subphases at a rather large, almost constant, tilt angle, both of which were experimentally confirmed unambiguously to exist [7,16–29,47,48]. They numerically calculated the subphase superlattice structures and their stability ranges in the g–T phase diagram by using the free energy

$$F = \sum_{i=1}^{N} (F_i + \Delta F_i). \tag{5}$$

Here, N is the total number of smectic layers, the polarization-independent part F_i given as

$$F_i = -\frac{\tilde{a}(T - T^*)}{T^*}(\cos\phi_{i-1,i} + \cos\phi_{i,i+1}) - \tilde{B}(\cos^2\phi_{i-1,i} + \cos^2\phi_{i,i+1}) \tag{6}$$

is an extension of Eq. (1) to include subphases as well as the main phases SmC^*_A and SmC^*, and the polarization-dependent part ΔF_i is written as

$$\Delta F_i = \frac{1}{2\chi}\left\{\mathbf{P}_i^2 + g(\mathbf{P}_{i-1}\cdot\mathbf{P}_i + \mathbf{P}_i\cdot\mathbf{P}_{i+1})\right\} + c_{\mathrm{p}}(\mathbf{P}_i\cdot\boldsymbol{\xi}_i) + c_{\mathrm{f}}\cos\theta(\mathbf{P}_i\cdot\Delta\mathbf{n}_{i\pm1}), \tag{7}$$

which consists of the last two terms containing the piezoelectric and flexoelectric coefficients c_{p} and c_{f}, as well as the polarization-polarization interactions. Only four dimensionless parameters are needed in their calculations: $\tilde{T} \equiv \tilde{a}\,(T - T^*)/(\tilde{B}\,T^*)$, the dimensionless temperature; $\chi c_{\mathrm{p}} c_{\mathrm{f}} \sin^2\theta\cos^2\theta/(2\tilde{B})$, the relative strength of the effective long-range interlayer interactions; g, the molecular positional correlation in adjacent layers; and $c_{\mathrm{f}}/c_{\mathrm{p}}$.

Figure 11 is a g–T phase diagram numerically recalculated by considering subphase superlattice structures up to 10 smectic layers so that we can include Sm$C^*_A(\frac{1}{4})$,

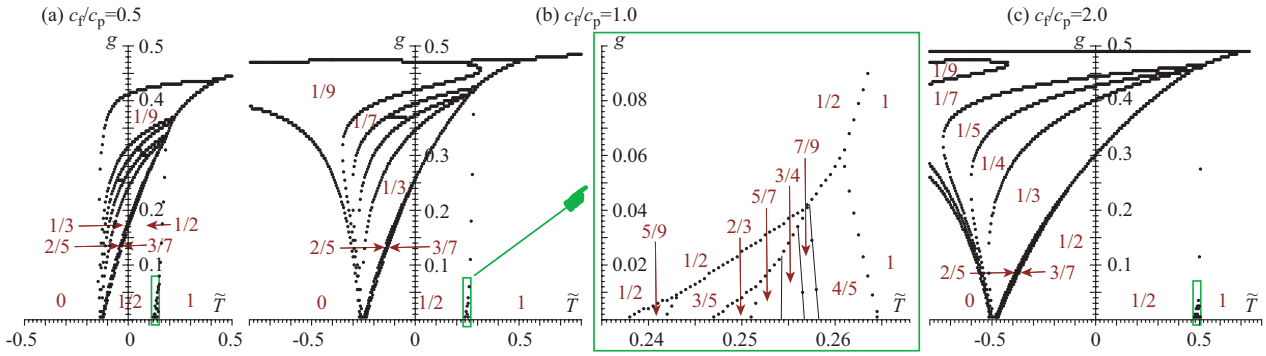

FIG. 11. (Color online) Recalculated g–$\tilde{T}$ phase diagrams with $\chi c_p c_f \sin^2\theta \cos^2\theta/(2\tilde{B}) = 0.12$ by taking account of superlattice structures consisting of up to 10 smectic layers, (a) $c_f/c_p = 0.5$, (b) $c_f/c_p = 1.0$, and (c) $c_f/c_p = 2.0$. Notice that $\frac{2}{5}$ and $\frac{3}{7}$ emerge between $\frac{1}{3}$ and $\frac{1}{2}$ and that several subphases also emerge in a very squeezed area above $q_T > \frac{1}{2}$ as illustrated in (b) Inset: All the subphases appear in the increasing order of q_T, but the ones with $\frac{1}{2} < q_T < 1$ are squeezed into an extremely narrow area so that the continuous change as observed in this paper could not be explained by the LRILIs. See text for details.

Sm$C_A^*(\frac{2}{5})$, Sm$C_A^*(\frac{3}{5})$, and Sm$C_A^*(\frac{2}{3})$ experimentally observed recently [17–19,47,48]. Here, q_T is used for specifying biaxial subphases, although the number of smectic layers in a unit cell was originally used [43]. Needless to say, the simplified phase diagram as illustrated in Fig. 11 is based on various approximations and hence can not explain all of the experimentally observed facts, as the intermolecular interactions in smectic liquid crystals are in fact so complicated. Conversely speaking, we can improve Fig. 11 in various ways by taking account of additional intermolecular interactions hitherto neglected. Aside from minor details, however, four important characteristic features of this phase diagram being observed are crucial to understanding the intriguing observations described in Sec. III: (i) the subphases emerge in the increasing order of q_T with temperature; (ii) all the subphases so far reported to exist can have some finite stability ranges; (iii) the stability ranges for the possible subphases with $0 < q_T \leqslant \frac{1}{2}$ are rather wide, whereas the ones with $\frac{1}{2} < q_T < 1$ are squeezed into an extremely narrow area; and (iv) the subphase with $q_T = \frac{1}{2}$, Sm$C_A^*(\frac{1}{2})$, is very special as compared with the others in the sense that the superlattice structure does not depend on g and that it is the subphase with $0 < q_T \leqslant \frac{1}{2}$ which exists stably for $g = 0$.

Now let us begin by considering to what extent we can understand the observed features described in Sec. III A, in particular, shown in Figs. 6 and 7. As q_T becomes smaller, superlattice structures resemble more and more SmC_A^* and their unit cells become larger and larger; hence, the difference in free energy between neighboring superlattice structures decreases with q_T and it may be difficult to locate the corresponding transition point. In real systems, such superlattice structures may also be suppressed by various factors including interface effects and thermal fluctuations. Actually, even a relatively weak influence of polarization fluctuations introduced by Prost and Bruinsma [8,9] effectively suppresses the transition points among the subphases with $q_T \leqslant \frac{1}{5}$ [49]; hence, the temperature change may look like continuous, for much more subphases may emerge if we take account of larger superlattice structures in the calculation. Experimentally, Sm$C_A^*(\frac{1}{4})$ was reported to exist in addition to well-known Sm$C_A^*(\frac{1}{3})$ and Sm$C_A^*(\frac{1}{2})$ [17–19]. Consequently, it is not unreasonable to consider that these three subphases are responsible for the two plateaux at 0.55 μm (79.9 °C–80.2 °C) and 0.73 μm (81.4 °C–81.7 °C) together with the bulge at around 1.0–1.5 μm (83 °C–86.5 °C) in Fig. 6(a), and that the apparent continuous change with temperature results from the polarization fluctuations. In fact, if we reasonably assume $p(\text{Sm}C_A^*) = 0.35$ μm and $p(\text{Sm}C^*) = 0.72$ μm (see Table I), we obtain, by using Eq. (4), 0.56 μm for Sm$C_A^*(\frac{1}{4})$, 0.7 μm for Sm$C_A^*(\frac{1}{3})$, and 1.4 μm for Sm$C_A^*(\frac{1}{2})$, respectively. As explained in Sec. III A, however, these assignments have not been experimentally confirmed yet.

It may be possible to understand similarly the high-temperature side with $q_T > \frac{1}{2}$, for there emerge several subphases in the order of increasing q_T with temperature as illustrated in Fig. 11. Notice, however, that the subphase stability ranges are squeezed into an extremely narrow area, and that any plateaux and bulges are not experimentally confirmed to emerge on the high-temperature side with $q_T > \frac{1}{2}$; it may be worth considering another possible degeneracy lifting due to thermal fluctuations. Intriguingly, in fact, the full-pitch band grows gradually in the apparent SmC^* region

TABLE I. Parameters used for reproducing the observed Bragg reflection peak versus temperature on the high-temperature side of the pitch divergence. As seen in Fig. 4(a), the SmC_A^* Bragg reflection band of 0.00 wt% (pure MC881) is very close to the intrinsic absorption of the liquid crystal sample; in 52.51 and 53.74 wt%, we could not observe any peak and hence assumed that the band is just buried in the intrinsic absorption with a peak at 0.35 μm. The peak of the SmC^* band is temperature dependent and we used the peak value just after the divergence (see Fig. 13).

Concentrations (wt%)	$p(\text{Sm}C_A^*)$[a] (μm)	$p(\text{Sm}C^*)$[b] (μm)	T_c (K)	α^* (erg K^{-1})
53.74	0.35	−0.72	360.0	9.9×10^{-14}
57.50	0.35	−0.71	347.3	3.8×10^{-14}

[a]Right-handed helix.
[b]Left-handed helix.

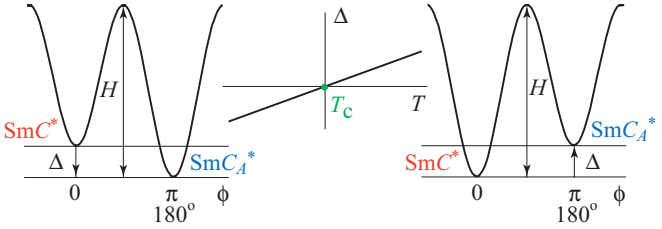

FIG. 12. (Color online) Schematic illustration of free energy density as a function of the azimuthal angle difference of the in-layer directors between adjacent layers given by Eq. (1).

as the temperature increases as illustrated in Figs. 6(c) and 9(c). We can hardly explain this continuous buildup of the full-pitch band in terms of the sequential emergence of subphases due to the LRILIs even if we take into account the blurring of the transition points among them caused by the polarization fluctuations. In this way, the degeneracy lifting directly caused by thermal fluctuations was taken into consideration successfully in the 53.74 wt% mixture in the previous preliminary report [31]. Now let us discuss the more details about this degeneracy lifting in several mixtures near critical concentration r_c.

B. Degeneracy lifting due to thermal fluctuations

As already outlined at the beginning of this paper, the phase transition between SmC_A^* and SmC^* has been treated by simply considering the free energy density given in Eq. (1) and illustrated in Fig. 12. The parameter values in Eq. (1) can be estimated experimentally. In fact, Song *et al.* studied the field-induced phase transition from SmC_A^* to SmC^* in the 20∼50 wt% mixtures, and determined α and H; they showed that α rapidly becomes smaller, but H does not change much as the MC452 concentration approaches the critical concentration $r_c \approx 59$ wt% [30]. They obtained $\alpha \approx 4 \times 10^3$ erg cm^{-3} K^{-1} (4×10^{-18} erg molecule^{-1} K^{-1}) and $H \approx 3.5 \times 10^5$ erg cm^{-3} (3.5×10^{-16} erg molecule^{-1}) in the 42 wt% mixture. This corresponds to $\Delta \approx 8 \times 10^4$ erg cm^{-3} (8×10^{-17} erg molecule^{-1}) at $T - T_c = 20$ K. Thus, both Δ and H are at least 2∼3 orders of magnitude smaller than the thermal energy $k_B T/(\textit{volume per molecule}) \approx 5 \times 10^7$ erg cm^{-3} (5×10^{-14} erg molecule^{-1}) at $T_c = 350$ K. Since the well-established tilted smectic structure, in fact, suppresses the thermal excitation of cooperative director motion of the antiphase mode which promotes the transition between SmC_A^* and SmC^*, we usually resort to the absolute zero temperature approximation and do not consider any thermal linkage between the two minima.

It should be noticed, however, that the phase transition between SmC_A^* and SmC^* induced not only by electric field but also by temperature actually occurs through solitary wave propagation in a nonuniform defect-assisted way but not through the antiphase mode in a uniform way [3,50–53]. Near the critical concentration, the free energy difference between the minima must be extremely small in a very wide temperature range; hence, solitary waves moving around dynamically may link these two minima thermally. We can now consider such a system consisting of N smectic layer boundaries, each of which takes either of the synclinic ferroelectric or anticlinic antiferroelectric ordering. Suppose this thermal linkage establishes a thermal equilibrium between the orderings, it is natural to consider that the ratio between $[A]$ and $[F]$ is given by the Boltzmann distribution [31]

$$\frac{[A]}{[F]} = \exp\left(-\frac{\Delta E}{k_B T}\right), \tag{8}$$

where ΔE is usually considered to change linearly with temperature near the frustration point

$$\Delta E = E_A - E_F = \alpha^*(T - T_c). \tag{9}$$

Equation (9) apparently looks the same as the free energy difference between $\phi = 0^\circ$ and 180° in Eq. (1), but the physical meaning is different. The point is that Eq. (1) is the free energy density, whereas Eq. (9) is the potential energy difference between the synclinic ferroelectric and anticlinic antiferroelectric orderings. The potential energy barrier between the orderings can be considered exceedingly high as compared with the thermal energy $k_B T$, for the actual number of molecules participating in the nonuniform defect-assisted change between the orderings must still be very large; by neglecting the ϕ distribution around the minima, therefore, the Boltzmann distribution can be treated in the one-dimensional (1D) Ising model, where no phase transition occurs as is well known.

It is not easy to determine T_c and α^* in Eqs. (8) and (9) *a priori*; here, we consider them as phenomenological adjustable parameters and try to explain the divergence of the peak wavelength and the gradual growth (disappearance) of the full-pitch band. At least approximately, the macroscopic helical pitch of a superlattice structure $p[\text{Sm}C_A^*(q_T)]$ is uniquely determined by q_T as given in Eq. (4). Using Eqs. (2), (8), and (9), we obtain

$$q_T = \frac{1}{1 + \exp\{-(\alpha^*/k_B)(T - T_c)/T\}}. \tag{10}$$

By combining Eqs. (4) and (10), the experimentally observed Bragg reflection peak versus temperature, at least on the high-temperature side of the pitch divergence, is rather well reproduced as illustrated in Fig. 13. The parameters used are listed in Table I; it is reasonable that T_c becomes lower and α^* decreases as the MC452 concentration increases toward the critical concentration r_c. For 53.74 wt%, the calculated curve fits the experimental data rather well even in the longer-wavelength region on the low-temperature side of the divergence as seen in Fig. 13(a); it does not reproduce the shorter-wavelength region with the bulge and the plateaux. This probably implies that the LRILIs do play a crucial role in the temperature region where the stable temperature ranges for the possible subphases with $0 < q_T \leqslant \frac{1}{2}$ are rather wide as shown in Fig. 11. In the temperature region where the possible subphases with $\frac{1}{2} < q_T < 1$ are squeezed into an extremely narrow area, on the other hand, it is safely concluded that degeneracy lifting is mainly due to thermal fluctuations.

Now, let us consider how can we explain the gradual growth of the full-pitch band in the apparent SmC^* temperature region. A solitary wave propagation causes a simultaneous change in the tilting sense of some neighboring layers and produces a pair of π-disclination defects. Aside from the tilting sense, a π-disclination defect changes the local

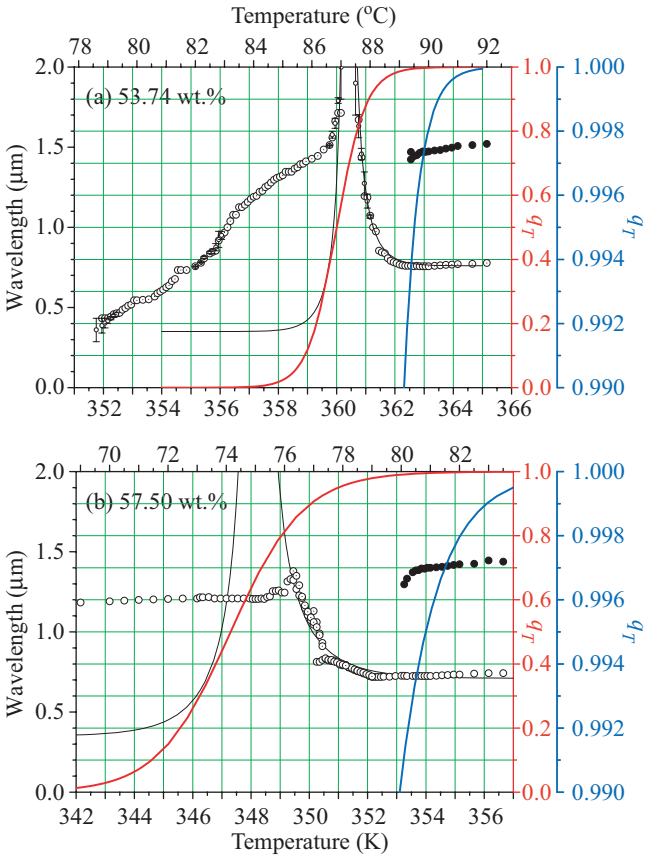

FIG. 13. (Color online) Observed Bragg reflection peak vs temperature in (a) 53.74 wt% and (b) 57.50 wt%, which is fitted by Eq. (4) together with Eq. (10) by using parameters listed in Table I; the high-temperature side is rather well reproduced as indicated by black thin curves. Red and blue thick curves showing q_T as a function of temperature T are plotted using the inside (red) scale and the expanded outside (blue) scale of q_T, respectively; the observed full-pitch band starts to grow at around $q_T \approx 0.991$.

periodicity from P to $P/2$. The introduced half-pitch $P/2$ may reduce the intensity of the full-pitch band because of the dispersion relation explained in Fig. 1. Therefore, it is anticipated that the intensity of the full-pitch band much more critically depends on the number of of defects than that of the half-pitch band. To understand the details, we need to perform numerical simulations. Anticlinic ordering defects are dynamically created and annihilated as pairs in the otherwise synclinic ordering prevailing throughout the bulk. The defect pairs must be distributed randomly throughout the bulk and their average number is

$$\tfrac{1}{2}(1 - q_T), \tag{11}$$

where q_T is given as a function of T in Eq. (10). The only additional parameter necessary to simulate the superlattice structure at T is the defect separation of a pair

$$n = \lfloor |x + 0.5| \rfloor \tag{12}$$

in the unit of the number of smectic layers, where x is assumed to be given by random numbers distributed normally with mean

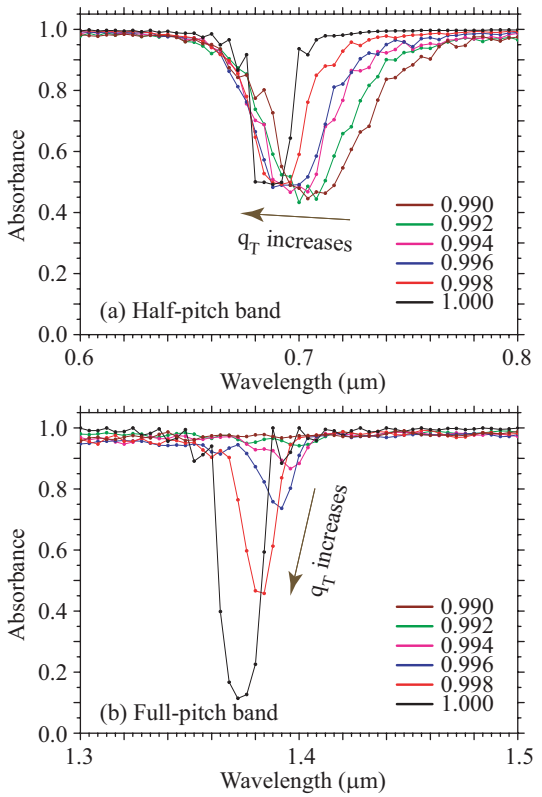

FIG. 14. (Color online) Simulated Bragg reflection spectra in a homogeneous cell with 15 000 smectic layers with 3.5 nm thickness for a light beam incident at 20° by changing the wavelength from 0.35 to 2.5 μm at 4-nm intervals. Parameters used are $\mu = 200$ and $\sigma = 50$; values given in the figure are those of q_T.

μ and standard deviation σ smectic layers

$$\frac{1}{\sqrt{2\pi}\sigma} \exp\left\{-\frac{(x-\mu)^2}{2\sigma^2}\right\}. \tag{13}$$

We have calculated the Bragg reflection spectra by using Berreman's 4×4 matrix method for randomly produced 10 superlattice structures and averaged them. Actual calculations were performed by SCILAB software in a homeotropic cell consisting of 15 000 smectic layers with 3.5 nm thickness for a light beam incident at an angle of 20° by changing the wavelength from 0.35 to 2.5 μm at 4-nm intervals.

Figure 14 illustrates the results with $\mu = 200$ and $\sigma = 50$, which successfully reproduces the growth of the full-pitch band at around $q_T \approx 0.991$. With decreasing either μ or σ, the growth starts to occur at smaller q_T; the results with $\mu = 200$ and $\sigma = 1$ look rather similar to Fig. 14, but $\mu = 100$ and $\sigma = 1$ give too small q_T, whereas $\mu = 500$ and $\sigma = 1$ predict too large q_T necessary for starting the growth. Since the superlattice structures are intrinsically disordered, the calculated Bragg reflection bands, both half and full pitch, do not appear to be smooth, but are rather observed wavy. The observed characteristic asymmetrical band shape of the full-pitch bands tailing toward the shorter-wavelength side is well reproduced; in particular, as q_T decreases, some reflection peaks, although small, may emerge in the wavelength region between the full-pitch band and the half-pitch band, as clearly seen by comparing Figs. 6(c) and 9(c) with Fig. 14. Regarding

the peak shift with q_T, the calculated results are just opposite to the observed ones. This discrepancy mainly results from the assumption in Eq. (4) that $p(\mathrm{Sm}C_A^*)$ and $p(\mathrm{Sm}C^*)$ do not depend on temperature. If we carefully compare calculated solid lines with observed open circles, we notice that the calculated values decrease while the observed ones increase with increasing q_T in the full-pitch growing regions in Fig. 13. In this way, the analysis based on the degeneracy lifting due to thermal fluctuations allows us to determine T_c and α^* and to explain the characteristic growth of the full-pitch band at around $q_T \approx 0.991$ in (A) low- and (B) intermediate-concentration regions.

The divergence is conspicuously observed in 52.51 and 53.74 wt%, but becomes less obvious as the MC452 concentration increases, and finally could not be seen for higher concentrations. It is impractical to determine T_c and α^* experimentally in (C) high-concentration region. And hence we try to consider qualitatively to what extent we can understand the big picture of the observed Bragg reflection spectra at various temperatures near the critical concentration r_c in terms of the degeneracy lifting due to thermal fluctuations. The bulk phase diagram of MC881 and MC452 binary mixture system indicates that the $\mathrm{Sm}C_A^*$ minimum at $\phi = 180^\circ$ is not the global minimum even at absolute zero temperature at or above r_c; a remarkable change is expected to occur in the Bragg reflection spectra. In fact, such a change is observed between (B) intermediate- and (C) high-concentration regions as described in detail in Sec. III. The near-IR Bragg reflection band at around 1.05–1.2 μm (30 °C–75 °C) in 57.50 wt% shown in Fig. 9(a) must be closely related with the presence of the $\mathrm{Sm}C_A^*$ global minimum at $\phi = 180^\circ$. It is not impertinent to consider that its disappearance in 57.79 wt% shown in Fig. 9(b) results from the fact that the $\mathrm{Sm}C_A^*$ minimum at $\phi = 180^\circ$ does not become the global minimum even at absolute zero temperature. The critical concentration r_c must be located between 57.50 and 57.79 wt%. The MC452 concentration of 57.79 wt% appears to be quite close to r_c, for the 57.79 wt% mixture shows the broadest half- and full-pitch bands and the widest growth temperature range of the full-pitch band as denoted in Sec. III C. In Eq. (9), we may say $T_c \approx 0$ and that α^* is extremely small. As the concentration increases further above r_c, the degeneracy lifting due to thermal fluctuations, i.e., the Boltzmann distribution given by Eq. (8), must still play an important role, although the linear approximation given by Eq. (9) may not hold for $T_c < 0$. In fact, the growth of the full-pitch band is observed in 58.12 and 58.74 wt% as seen in Fig. 4, but the detailed studies have not yet been carried out.

C. Interplay between LRILIs and thermal fluctuations

In spite of the success on the high-temperature side of the divergence, Eqs. (4) and (10) could hardly reproduce the experimentally observed peak wavelength versus temperature curve on the low-temperature side of the divergence, except for the longer-wavelength part corresponding to the narrow temperature region of $q_T > \frac{1}{2}$ in Fig. 13(a). The effective LRILIs may produce a variety of subphases in a wide temperature region of $0 < q_T \leqslant \frac{1}{2}$ as illustrated in Fig. 11. The number of emerging subphases may further increase if larger unit cells are taken into consideration and the difference in free energy between them decreases accordingly. Among them, the stable existence of $\mathrm{Sm}C_A^*(\frac{1}{3})$ and $\mathrm{Sm}C_A^*(\frac{1}{2})$ was firmly established by RXS experiments. Although it has not been confirmed by RXS as yet, $\mathrm{Sm}C_A^*(\frac{1}{4})$ was concluded to emerge in a few materials by observing Bragg reflection due to the long-pitch helical structure and/or EFIB [17–19]. Moreover, it has been well established in a wide range of materials that $\mathrm{Sm}C_A^*(\frac{1}{3})$ shows a characteristic valley (the most easily deformable region) in the E–T phase diagram with EFIB contours. Taking account of all these facts, it is crucial to know whether the EFIB valley corresponds to the bulge or the 0.75-μm plateau in Fig. 6, but still there remains some uncertainty as explained in Sec. III A.

Anyway, the Bragg reflection peak apparently changes continuously across these plateaux and bulge. So long as the subphase region $0 < q_T < \frac{1}{3}$ is concerned, the apparent continuous change, i.e., blurring of the transition temperatures among the subphases, may be explained by the polarization fluctuations [8,9] as mentioned in Sec. IV A. The blurring of much stabler $\mathrm{Sm}C_A^*(\frac{1}{3})$ and $\mathrm{Sm}C_A^*(\frac{1}{2})$ can hardly be ascribed to the same mechanism. Because of the success in the high-temperature region of $q_T > \frac{1}{2}$, the thermal fluctuations, i.e., dynamically moving around solitary waves, must also be effective for lifting the degeneracy in the low-temperature region of $0 < q_T \leqslant \frac{1}{2}$. Therefore, it is natural to consider that the interplay between the thermal fluctuations and the LRILIs is responsible for the observed characteristic, apparently continuous change of the Bragg reflection band on the low-temperature side of the divergence where the plateaux and bulge are observed as in Fig. 6. This is an important and interesting problem to be studied theoretically in the near future.

Now, let us consider what is happening in Sec. III B intermediate concentration region. Figure 8 indicates that, as the concentration increases, the bulge grows into the near-IR band in the intermediate region. What mechanism stabilizes the bulge? Since the concentration is immediately below the critical one r_c, one of the stable subphases must be responsible for the near-IR Bragg reflection band in a very wide temperature range. Two conceivable stable subphases are $\mathrm{Sm}C_A^*(\frac{1}{3})$ and $\mathrm{Sm}C_A^*(\frac{1}{2})$. Experimentally, $\mathrm{Sm}C_A^*(\frac{1}{3})$ is stabler than $\mathrm{Sm}C_A^*(\frac{1}{2})$ in some materials [13] and vice versa in some others [54]. In the calculated g–$\tilde{T}$ phase diagram shown in Fig. 11, $\mathrm{Sm}C_A^*(\frac{1}{2})$ is much stabler than $\mathrm{Sm}C_A^*(\frac{1}{3})$. As already pointed out, however, the vertical flexoelectric polarization effect, which is neglected in the above calculation, may destroy $\mathrm{Sm}C_A^*(\frac{1}{2})$ so that it does not emerge in some materials [55]. In this way, it is not easy to decide *a priori* which is stabler, $\mathrm{Sm}C_A^*(\frac{1}{3})$ or $\mathrm{Sm}C_A^*(\frac{1}{2})$. Here, we pay particular attention to the very characteristic feature of the phase diagram shown in Fig. 11, and assume that the bulge is closely related with $\mathrm{Sm}C_A^*(\frac{1}{2})$. Note that $\mathrm{Sm}C_A^*(\frac{1}{2})$ is the only subphase that may stably exist at $g = 0$ in a wide temperature range. The interlayer positional correlation g is considered to be much smaller in $\mathrm{Sm}C^*$ than in $\mathrm{Sm}C_A^*$ [4,55]. As the concentration increases and approaches the critical one r_c, the stability of $\mathrm{Sm}C_A^*$ and hence g may come to decrease tremendously. Thus, $\mathrm{Sm}C_A^*(\frac{1}{2})$ may become exceptionally stable as compared to the others so that it may be observed mainly in a wide

temperature range. Suppose this scenario is realized, Sm$C_A^*(\frac{1}{3})$ may not emerge at least at $E = 0$. Unfortunately, we have not obtained the E–T phase diagram with EFIB contours in 54.99 and 57.50 wt%. The emergence of Sm$C_A^*(\frac{1}{3})$ in 54.37 wt% as shown in Fig. 10 does not cause any difficulties, as this concentration is just transitional and in fact the Bragg reflection spectra are not single-bell-shaped bands in the range of 56 °C–77 °C as explained in Sec. III B and shown in Fig. 8.

Figures 4 and 8 also indicate that the near-IR band at around 1.05–1.1 μm (30 °C–49 °C) in 53.74 wt% grows into the near-IR Bragg reflection spectra at around 1.05–1.35 μm (30 °C–84.5 °C) in 54.37, 54.99, and 57.50 wt%; hence, the near-IR band in the intermediate region has a close resemblance to the band in 53.74 wt%, i.e., not only to the band at around the 1.0–1.5 μm (83 °C–86.5 °C) bulge but also to the band at around 1.05–1.1 μm (30 °C–49 °C) in Figs. 4(a) and 8(a). A big question is what causes the near-IR band at around 1.05–1.1 μm (30 °C–49 °C) in 53.74 wt%. Since the band emerges on the low-temperature side of SmC_A^*, we need to introduce some additional SRILIs other than those stabilizing the main phases, SmC_A^* and SmC^*, in addition to the LRILIs responsible for the degeneracy lifting to produce several subphases; a resultant additional phase must be a ferroelectric hexatic phase or reentrant SmC^* [56–58]. The frustration between either of these and SmC_A^* may produce some superlattice structures very close to Sm$C_A^*(\frac{1}{2})$ or Sm$C_A^*(\frac{1}{3})$. This is just a rough outline regarding how to understand the Bragg reflection spectra at low temperatures and the detailed study may become a challenging task for future experimental and theoretical works.

ACKNOWLEDGMENTS

Mitsubishi Gas Chemical Company, Inc., is acknowledged for the gift of liquid crystal compounds, and the Irish Research Council of Science, Engineering and Technology is thanked for support to K. L. Sandhya as a post-doctoral fellow. The laboratory facilities were equipped with a grant from the Science Foundation of Ireland. Visit of K.L.S. to Dublin was facilitated through Ireland-India cooperation funding; J.K.V. thanks the Dean of FEMS, Trinity College Dublin for financial support. K. Ishikawa gratefully acknowledges financial support of Grants-in Aid for Science Research (B) (23310072) and Bilateral Joint Projects/Seminars by JSPS.

[1] A. D. L. Chandani, E. Gorecka, Y. Ouchi, H. Takezoe, and A. Fukuda, Jpn. J. Appl. Phys. **28**, L1265 (1989).
[2] H. Orihara and Y. Ishibashi, Jpn. J. Appl. Phys. **29**, L115 (1990).
[3] J.-K. Song, A. Fukuda, and J. K. Vij, Phys. Rev. Lett. **101**, 097801 (2008).
[4] M. A. Osipov and A. Fukuda, Phys. Rev. E **62**, 3724 (2000).
[5] J. Li, H. Takezoe, and A. Fukuda, Jpn. J. Appl. Phys. **30**, 532 (1991).
[6] P. Gisse, V. L. Lorman, J. Pavel, and H. T. Nguyen, Ferroelectrics **178**, 297 (1996).
[7] J. P. F. Lagerwall, F. Giesselmann, and M. Osipov, Liq. Cryst. **33**, 625 (2006).
[8] J. Prost and R. Bruinsma, Ferroelectrics **148**, 25 (1993).
[9] R. Bruinsma and J. Prost, J. Phys. (France) **4**, 1209 (1994).
[10] P. Bak, Phys. Today **39**(12), 38 (1986).
[11] T. Isozaki, T. Fujikawa, H. Takezoe, A. Fukuda, T. Hagiwara, Y. Suzuki, and I. Kawamura, Jpn. J. Appl. Phys., Part 2 **31**, L1435 (1992).
[12] T. Isozaki, T. Fujikawa, H. Takezoe, A. Fukuda, T. Hagiwara, Y. Suzuki, and I. Kawamura, Phys. Rev. B **48**, 13439 (1993).
[13] A. Fukuda, Y. Takanishi, T. Isozaki, K. Ishikawa, and H. Takezoe, J. Mater. Chem. **4**, 997 (1994).
[14] C. D. Cruz, J. C. Rouillon, J. P. Marcerou, N. Isaert, and H. T. Nguyen, Liq. Cryst. **28**, 125 (2001).
[15] J. P. F. Lagerwall, P. Rudquist, S. T. Lagerwall, and F. Giesselmann, Liq. Cryst. **30**, 399 (2003).
[16] J. P. Marcerou, H. T. Nguyen, N. Bitri, A. Gharbi, S. Essid, and T. Soltani, Eur. Phys. J. E **23**, 319 (2007).
[17] A. D. L. Chandani, N. M. Shtykov, V. P. Panov, A. V. Emelyanenko, A. Fukuda, and J. K. Vij, Phys. Rev. E **72**, 041705 (2005).
[18] K. L. Sandhya, J. K. Vij, A. Fukuda, and A. V. Emelyanenko, Liq. Cryst. **36**, 1101 (2009).
[19] K. L. Sandhya, A. Fukuda, and J. K. Vij, Mol. Cryst. Liq. Cryst. **511**, 36 (2009).
[20] P. Mach, R. Pindak, A.-M. Levelut, P. Barois, H. T. Nguyen, C. C. Huang, and L. Furenlid, Phys. Rev. Lett. **81**, 1015 (1998).
[21] P. Mach, R. Pindak, A.-M. Levelut, P. Barois, H. T. Nguyen, H. Baltes, M. Hird, K. Toyne, A. Seed, J. W. Goodby *et al.*, Phys. Rev. E **60**, 6793 (1999).
[22] L. S. Hirst, S. J. Watson, H. F. Gleeson, P. Cluzeau, P. Barois, R. Pindak, J. Pitney, A. Cady, P. M. Johnson, C. C. Huang *et al.*, Phys. Rev. E **65**, 041705 (2002).
[23] A.-M. Levelut and B. Pansu, Phys. Rev. E **60**, 6803 (1999).
[24] P. Fernandes, P. Barois, E. Grelet, F. Nallet, J. W. Goodby, M. Hird, and J.-S. Micha, Eur. Phys. J. E **20**, 81 (2006).
[25] S. Jaradat, P. D. Brimicombe, C. Southern, S. D. Siemianowski, E. DiMasi, M. Osipov, R. Pindak, and H. F. Gleeson, Phys. Rev. E **77**, 010701(R) (2008).
[26] T. Akizuki, K. Miyachi, Y. Takanishi, K. Ishikawa, H. Takezoe, and A. Fukuda, Jpn. J. Appl. Phys., Part 1 **38**, 4832 (1999).
[27] P. M. Johnson, D. A. Olson, S. Pankratz, T. Nguyen, J. Goodby, M. Hird, and C. C. Huang, Phys. Rev. Lett. **84**, 4870 (2000).
[28] A. Cady, J. A. Pitney, R. Pindak, L. S. Matkin, S. J. Watson, H. F. Gleeson, P. Cluzeau, P. Barois, A.-M. Levelut, W. Caliebe, J. W. Goodby, M. Hird, and C. C. Huang, Phys. Rev. E **64**, 050702(R) (2001).
[29] I. Musevic and M. Skarabot, Phys. Rev. E **64**, 051706 (2001).
[30] J. K. Song, A. Fukuda, and J. K. Vij, Phys. Rev. E **78**, 041702 (2008).
[31] K. L. Sandhya, A. D. L. Chandani-Perera, A. Fukuda, J. K. Vij, and K. Ishikawa, Europhys. Lett. **90**, 56005 (2010).
[32] D. W. Berreman, Mol. Cryst. Liq. Cryst. **22**, 175 (1973).
[33] K. Hori, Mol. Cryst. Liq. Cryst. **100**, 75 (1983).
[34] Y. Ouchi, T. Shingu, H. Takezoe, A. Fukuda, E. Kuze, M. Koga, and N. Goto, Jpn. J. Appl. Phys. **23**, L660 (1984).

[35] T. Matsumoto, A. Fukuda, M. Johno, Y. Motoyama, T. Yui, S.-S. Seomun, and M. Yamashita, J. Mater. Chem. **9**, 2051 (1999).
[36] M. Takeuchi, K. Chao, T. Ando, T. Matsumoto, A. Fukuda, and M. Yamashita, Ferroelectrics **246**, 1 (2000).
[37] Y. Yoshioka, M. Johno, T. Yui, and T. Matsumoto, Euro. Pat. Appl. EP1039329 (2000).
[38] J.-K. Song, A. D. L. Chandani, A. Fukuda, J. K. Vij, I. Kobayashi, and A. V. Emelyanenko, Phys. Rev. E **76**, 011709 (2007).
[39] N. M. Shtykov, A. D. L. Chandani, A. V. Emelyanenko, A. Fukuda, and J. K. Vij, Phys. Rev. E **71**, 021711 (2005).
[40] M. Yamashita and S. Miyazima, Ferroelectrics **148**, 1 (1993).
[41] A. Roy and N. V. Madhusudana, Europhys. Lett. **36**, 221 (1996).
[42] P. V. Dolganov, V. M. Zhilin, V. K. Dolganov, and E. I. Kats, Phys. Rev. E **67**, 041716 (2003).
[43] A. V. Emelyanenko and M. A. Osipov, Phys. Rev. E **68**, 051703 (2003).
[44] M. B. Hamaneh and P. L. Taylor, Phys. Rev. Lett. **93**, 167801 (2004).
[45] P. V. Dolganov, V. M. Zhilin, V. K. Dolganov, and E. I. Kats, Phys. Rev. E **86**, 020701(R) (2012).
[46] T. Y. Tan, L. H. Ong, and M. Cepic, Mol. Cryst. Liq. Cryst. **540**, 69 (2011).
[47] S. Wang, L. D. Pan, R. Pindak, Z. Q. Liu, H. T. Nguyen, and C. C. Huang, Phys. Rev. Lett. **104**, 027801 (2010).
[48] A. D. L. Chandani, A. Fukuda, S. Kumar, and J. K. Vij, Liq. Cryst. **38**, 663 (2011).
[49] A. V. Emelyanenko and M. A. Osipov, Ferroelectrics **309**, 13 (2004).
[50] J.-F. Li, X.-Y. Wang, E. Kangas, P. L. Taylor, C. Rosenblatt, Y. I. Suzuki, and P. E. Cladis, Phys. Rev. B **52**, 13075(R) (1995).
[51] L. A. Parry-Jones and S. J. Elston, Phys. Rev. E **63**, 050701(R) (2001).
[52] L. A. Parry-Jones and S. J. Elston, Appl. Phys. Lett. **79**, 2097 (2001).
[53] J.-K. Song, A. Fukuda, and J. K. Vij, Phys. Rev. E **76**, 011708 (2007).
[54] B. K. McCoy, Z. Q. Liu, S. T. Wang, L. Pan, S. Wang, H. T. Nguyen, R. Pindak, and C. C. Huang, Phys. Rev. E **77**, 061704 (2008).
[55] A. V. Emelyanenko, A. Fukuda, and J. K. Vij, Phys. Rev. E **74**, 011705 (2006).
[56] S.-S. Seomun, T. Gouda, Y. Takanishi, K. Ishikawa, H. Takezoe, and A. Fukuda, Liq. Cryst. **26**, 151 (1999).
[57] V. Novotna, M. Glogarova, V. Hamplova, and M. Kaspar, J. Chem. Phys. **115**, 9036 (2001).
[58] R. Korlacki, A. Fukuda, and J. K. Vij, Europhys. Lett. **77**, 36004 (2007).